Article:
López, A, Vivacqua, V, Hammond, R et al. (2020) Analysis of screw feeding of faceted particles by discrete element method. Powder Technology, 367. pp. 474-486. ISSN: 0032-5910

https://doi.org/10.1016/j.powtec.2020.03.064

Analysis of Screw Feeding of Faceted Particles by Discrete Element Method

Alejandro López[1], Vincenzino Vivacqua[2], Robert Hammond, Mojtaba Ghadiri*

School of Chemical and Process Engineering, University of Leeds, Leeds, UK

*Corresponding author: Mojtaba Ghadiri, e-mail: m.ghadiri@leeds.ac.uk

Abstract

Reliable and consistent powder flow in screw feeders is of great interest to a wide range of industries, particularly for continuous manufacturing of pharmaceutical powders. However, analysis of flow of cohesive powders with sharp corners and edges, as commonly found in the case of crystalline solids, presents a great challenge due to complexity of shape and its influence on flow. In the present work, the influence of particle shape and cohesion on phenomena such as cohesive arching in hoppers and screw feeder pitches is analysed by numerical simulations using the Discrete Element Method, and their impact on the outlet mass flow rate is evaluated. Faceted and spherical particles with different cohesion levels are generated and allowed to settle in a hopper on top of a screw feeder. The screw is then rotated, thus feeding the particles through the barrel. Particle interactions are analysed numerically for the hopper region, a predominantly slow-flow regime, and for the pitches of the screw feeder, where a speed-dependent regime prevails.

Paracetamol crystal shape is taken as a model faceted shape. Its parameters such as the coefficients of restitution and friction, needed for the simulations, are calibrated by experimental work.

Transient arching occurs as the level of cohesion is increased. The frequency of formation and collapse of arches within the hopper region increases, and eventually, permanent arching is

[1]Current address: University of Deusto, Avenida de las Universidades 24, Bilbao, 48007, Spain
[2]Curent address: Johnson Matthey, Belasis Avenue, Billingham, TS23 1LB, United Kingdom

observed. Analysis of stress and strain rate in the screw barrel region shows that the shear stress is a weak function of the shear rate with a power index of around 0.3, which is independent of particle shape. The flow rate is influenced considerably by particle shape, whilst increased cohesion causes an increase in void fraction and affects transient arching.

Keywords

DEM, Screw Feeder, Cohesion, Faceted particles, Powder Flow

1. Introduction

Screw feeders are commonly used in many industries handling and processing powders and grains. This type of feeder is important because it provides a relatively controllable mass flow rate for free-flowing powders [1]. However, fine and cohesive powders tend to cause rat holing and arching [1]. Early studies on the design of mass flow silos and solids handling equipment were carried out by Jenike [2,3], in which stresses at the outlet of hoppers were calculated and the arch span predicted. In his work as well as in Walker's study of pressure distribution and arching [4], the underlying assumption was that powder strength is dependent only on the local stresses in the bulk powder before arching. Based on the same continuum mechanics approach, Enstad [5] analysed arching in hoppers, making a number of assumptions, some of which were not easily verifiable, such as the angle of the footing of the arch on the hopper wall. He developed a model predicting the critical outlet width, for which the powder transitions between arching and flow. His model is more refined than those of previous studies, but still requires bulk powder characterisation. Pharmaceutical powders are highly diverse in bulk properties, and at the early stages of development of new Active Pharmaceutical Ingredients (API), very little powder quantity is available for their bulk characterisation for flowability. Therefore, the ability to predict bulk flow properties from individual particles of an API is

highly desirable. This is possible in principle by numerical simulations by the Discrete Element Method, although the use of fine particles in the micrometre size range in the simulations is still very challenging. Nevertheless, by reproducing the conditions leading to arching in hoppers by DEM simulations, a deeper understanding of how transient arching affects the mass flow rate as well as the conditions leading to arching can be achieved. Hou *et al.* [1] carried out a DEM study of the flow of spherical particles, which were cohesive, in a screw feeder. However, crystals have faceted shapes and are not well represented by spheres. The commercial software Rocky DEM ESSS, Brazil, can model faceted shapes and accounts for the interaction between the sharp edges and corners. The recent analysis by Vivacqua *et al.* [6] shows that faceted shapes have a strong influence on particle flow behaviour. Thus, this approach is used here to provide a more realistic analysis of flow of particles having such shapes, as relevant to crystalline structures commonly encountered in APIs.

The system studied in this work is divided into two distinct regions. The first region is that of the hopper on top of the screw feeder, where the flow regime is mainly quasi-static. The second region is the screw feeder, where the flow regime in the screw pitches is more dependent on the rotational speed of the screw. It can fall into the quasi-static flow regime at low speeds, where the shear stress is independent of strain rate [7], and into to the inertial regime if the rotational speed of the screw is high. Here, the powder flow is liquid-like and it has been modelled in a Eulerian frame as a Bingham fluid [8]. The friction coefficient in the rheological model developed by Jop *et al.* in [8] is a function of a single non-dimensional number called the Inertial number, I, given by equation 1. It represents the ratio between the inertial and the macroscopic deformation timescales.

$$I = \frac{|\dot{\gamma}|d}{\sqrt{\frac{P}{\rho_s}}} \tag{1}$$

$|\dot{\gamma}|$ is the second invariant of the strain rate tensor, d is the particle diameter, ρ_s is the particle density and P is the hydrostatic stress, which is calculated as the average of the three principal stresses.

The rheology of granular matter under dynamic conditions has been studied both experimentally as well as computationally by Tardos *et al.* [9]. They analysed granular flow in a Couette device, consisting of two concentric cylinders containing the powder to be analysed in the annular region, with the inner cylinder rotating and the outer one stationary. The shear stress was constant for different rotational speeds in the slow frictional regime. As the strain rate was increased by increasing the speed, the characteristics of the flow moved towards the intermediate and rapid flow regimes, i.e. the shear stress increased more rapidly at large strain rates. More recently, Berger *et al.* [10] have also studied dense granular cohesive flows under shear strains by means of contact dynamics simulations. They report that the bulk friction, described by the ratio of shear to normal stress, and bulk cohesion represented by a Coulomb-like functional form are both dependent on the strain rate. Also, they proposed a cohesive inertial number to unify the bulk behaviour for different adhesion and strain rate levels. However, validation of the predictions by comparison with experimental measurements has so far not been reported, presumably due to difficulty of testing. For quasi-static bulk powder failure characterisation, there are nowadays a wide range of methods available, such as the unconfined compression test [11], Edinburgh Powder Tester [12], Ball Indentation Method [13], Schulze Shear Cell [14], Jenike powder tester [3] and Environmental Caking Tester [15], Raining Bed Method [16], The Sevilla Powder Tester [17], Brookfield Powder Flow Tester [18], Hosokawa Micron Powder Tester PT-X [19], SSSpinTester-X Powder Strength Tester [20]. In contrast, for dynamic flow characterisation, the commercially available instruments are limited to Freeman Technology FT4 Rheometer [21] and Anton Paar Powder Rheometer [22], as otherwise it is difficult to operate shear cells under dynamic conditions. Recently

powder rheometry has been analysed to establish functional relationships between the torque and the work done on the powder and its bulk rheology ([22]-[30]). The aim of the work presented here is to analyse the flow behaviour of cohesive faceted particles inside a screw feeder and explore if its system dynamics can be correlated to the characteristic rheology, i.e. apparent shear viscosity and bulk friction and cohesion as a function of the strain rate, as obtained for example from the FT4 rheometer.

2. Model description

2.1. Discrete Element Modelling

In DEM, the motion of individual particles is obtained through numerical integration of the equations of motion for every individual particle. The forces acting on the particles are calculated accounting for both contact and body forces such as gravity, as Cundall and Strack first proposed in [31].

The translation and rotation of the individual particles are described by equations 2 and 3 [32]:

$$m_i \frac{d\boldsymbol{v}_i}{dt} = \sum \boldsymbol{F}_{C,i} + m_i \boldsymbol{g} + \boldsymbol{f}_{pf,i} \tag{2}$$

$$\frac{d(\boldsymbol{I}_i \boldsymbol{\omega}_i)}{dt} = \boldsymbol{R}_i (\sum \boldsymbol{M}_{C,i} + \boldsymbol{M}_{pf,i}) \tag{3}$$

where $\boldsymbol{I}_i$:moment of inertia, $\boldsymbol{\omega}_i$: angular velocity, m_i: particle mass, $\boldsymbol{v}_i$: translational velocity, $\boldsymbol{F}_{C,i}$: contact force, $\boldsymbol{f}_{pf,i}$: fluid-particle interaction force, $\boldsymbol{R}_i$: rotation matrix (from global to local coordinate system), $\boldsymbol{M}_{C,i}$: contact torque, $\boldsymbol{M}_{pf,i}$: torque due to fluid forces. In the current work, the interaction with the air has been neglected in all cases as the particles are large and hence the influence of air drag is negligible.

2.2. Contact model

Amongst the available contact models incorporating adhesion, Rocky DEM has Luding's adhesive contact model [34], which is the one selected in order to account for cohesive forces. This, so called, linear adhesive force model is defined by two parameters [32]:

- A minimum adhesive distance for which a force prevails at negative overlap, i.e. when the surfaces of the particles are not touching. It was set to zero in the cases analysed in this work.
- A stiffness ratio (or adhesive stiffness, K_{adh}), which is responsible for the cohesive force. Its effect on the force-overlap graph is shown in Figure 1.

Figure 1: Force-overlap graph for different values of the adhesive stiffness obtained in Rocky DEM for a spherical particle against a wall

In this adhesive elasto-plastic contact model the force increases with the overlap according to a linear relationship until the maximum overlap is reached. The slope of the unloading part is larger than the loading part and is generally dependent on the maximum overlap. The full original model, as described by Luding in [33] is shown in Figure 2.

Figure 2: Luding's elasto-plastic adhesive contact model redrawn from [29]

The corresponding piecewise-linear set of equations describing the model are shown in equation 4, where δ is the overlap, k_1 and k_2 are the loading and unloading stiffnesses, respectively, and k_{adh} is the adhesive stiffness. Here as well as in [33] f_0 is taken as zero and the values for negative overlap (describing the adhesive distance) are neglected, i.e. the value set for the adhesive distance is zero for the simulations carried out here.

$$f^{hys} = \begin{cases} k_1\delta & if\ k_2(\delta-\delta_0) \geq k_1\,\delta \\ k_2(\delta-\delta_0) & if\ k_1\delta > k_2(\delta-\delta_0) > -k_{adh}\delta \\ -k_c\delta & if -k_c\delta \geq k_2(\delta-\delta_0) \end{cases} \quad (4)$$

3. Rocky DEM offers the possibility of modelling faceted particles through polyhedral shapes. While for spherical particles, the contact plane is always perpendicular to the line connecting the centres, when non-rounded particles are considered, Rocky DEM calculates one of the following distances in order to assess the contact between them: closest point of two particles, closest point of a particle and a boundary triangle or, if there is physical contact, the points exhibiting the maximum overlap distance [32]. The contact plane will then be perpendicular to the line that connects those points. **Simulation parameters**

As outlined before, faceted particles were chosen for these simulations as the main aim of this research is to simulate the behaviour of API's with crystalline structures with different cohesion levels. In this particular case, the API modelled is paracetamol. However, both spherical particles as well as faceted particles with different values of the adhesive stiffness were simulated. The faceted shape used in the simulations is depicted in Figure 3(a) and an SEM micrograph of paracetamol crystals is shown in Figure 3(b) for comparison. The SEM images were taken with the Hitachi Benchtop TM3030 Scanning Electron Microscope. The computational particles are typically defined in Rocky DEM through a series of parameters, which are shown in Table 1.

Figure 3: (a) Shape of the faceted particles selected for the simulations in Rocky DEM and (b) SEM image of paracetamol crystals

Table 1: Parameters used for construction of the faceted particles

Regarding the simulation parameters, the material properties and interaction coefficients are given in Tables 2 and 3, respectively, while the particle size distribution is shown in Table 4. The coefficient of restitution was calibrated through high speed camera footage. Through image analysis, an average value for the coefficient of restitution was obtained by computing velocities before and after impact for Paracetamol particles. The static sliding friction coefficient was obtained by means of measuring the angle at which Paracetamol particles slide on a plane substrate of the materials of interest, i.e. glass and stainless steel while tilting it at very low speeds. The dynamic sliding friction coefficient was assumed equal to the static value. Since the aim is to compare different cohesion levels and particle shapes made of the same material, Young's modulus was reduced in order to be able to afford a longer time step and considerably increase the computational speed [33].

Table 2: Material properties for Paracetamol and stainless steel

Table 3: Interaction coefficients for particles and boundaries

Table 4: Cumulative particle size distribution

The geometry chosen for the simulations is that of a typical screw feeder and is shown in Figure 4. The inlet from which particles are released is situated in the upper part of the hopper and is represented as a red square in Figure 4.

Figure 4: Geometry of the screw feeder used in the simulations

Regarding the cohesive interactions between particles themselves and particles to boundary, the value for the adhesive stiffness was varied between 0 and 0.9. However, it was observed that, due to the nature of the contact model, if the adhesive stiffness was increased over 0.6, the particles were either expelled from the screw feeder as they were generated or stayed inside it indefinitely due to excessively high adhesion forces. Thus, only the simulations with adhesive stiffness values below 0.6 were considered. In addition, different screw angular speeds were simulated in order to assess the effect of the strain rate both on the powder flow regime as well as on arching.

4. Results and discussion

A series of simulations were set up for the screw feeder geometry shown in Figure 4 for different values of the adhesive stiffness and rotational speed. In the first part of the results,

the rheological characteristics of powder flow of the proposed faceted shapes in the screw feeder is presented in terms of the functional dependence of the shear stress on the strain rate and compared with those obtained from simulations of the Freeman FT4 powder rheometer. Thereafter, an in-depth analysis is carried out of the fluctuations in some of the most important variables of the screw feeder, such as mass flow rate, particle trajectories and velocities and power consumption as a function of adhesive stiffness and rotational speed of the screw. In the last part of the results an analysis is presented of transient arching and how it is affected by properties and conditions used in the simulations.

4.1. Powder flow in the screw feeder

In order to calculate the inertial number of the flow within the screw feeder, two measurement regions are considered, as depicted in Figure 5, for which the stress tensor is calculated. It is composed of two different contributions, one corresponding to the velocity fluctuations of the particles and another being the sum of the contact forces in the measurement bin. Equation 5 shows the mathematical expression for the averaged stress tensor.

$$\overline{\sigma_{ij}} = \frac{1}{2V}\sum_{N_p \in V} \frac{1}{2} m_p \delta v_i \delta v_j + \frac{1}{V}\sum_{N_c \in V} r_i^c \, F_j^c \tag{5}$$

where V is the measurement bin volume; m_p is the particle mass; δv_i and δv_j are the fluctuation velocities; F_j^c is the contact force at contact c and r_i^c is the position vector, N_p is the number of particles, N_c is the number of contacts and the sub-indices i and j represent the axes on which they are referenced.

Figure 5: Representation of the measurement volumes in the screw feeder

From the stress tensor, its principal components and invariants are obtained by means of exporting the control volume data from Rocky DEM to Microsoft Excel. Once these first and second invariants are obtained for each of the measurement bins, the hydrostatic and deviatoric stresses are defined according to equations 6 and 7, where σ_1, σ_2 and σ_3 are the eigenvalues of the stress tensor (or principal stresses) and I_1 and I_2 are the first and second invariants of the stress tensor, respectively. The hydrostatic and deviatoric stresses can then be calculated as shown in equations (6)-(7) [32]:

$$I_1 = \sigma_1 + \sigma_2 + \sigma_3$$

$$I_2 = \sigma_1\sigma_2 + \sigma_2\sigma_3 + \sigma_3\sigma_1$$

$$I_3 = \sigma_1\sigma_2\sigma_3 \tag{6}$$

$$\text{Deviatoric Stress } \tau_D = \frac{\sqrt{(\sigma_1-\sigma_2)^2+(\sigma_1-\sigma_3)^2+(\sigma_2-\sigma_3)^2}}{\sqrt{6}} = \sqrt{\frac{I_1^2}{3} - I_2} \tag{7}$$

Following this step, the Inertial number is calculated according to equation 1 once the strain rate is obtained. For simplicity, the latter is defined as the ratio between the average particle velocity inside the volume and the shear band width, which is assumed to be equal to five particle diameters [6, 35-38].

The shear stress may be made non-dimensional by dividing it by the inertial stress as done previously by Vivacqua *et al.* in [6], represented by equation (8). The resulting non-dimensional stress is shown in equation (9).

$$Inertial\ stress = \rho_p d_p^2 \gamma^2 \quad (8)$$

$$Non-dimensional\ stress = \frac{\tau}{\rho_p d_p^2 \gamma^2} \quad (9)$$

The non-dimensional shear stress is expressed as a function of the Inertial number. The results are shown in Figure 6, where an almost perfect collapse for all the cases of faceted particles with different surface energies and at different rotational speeds is observed.

Figure 6: Non-dimensional stress as a function of the Inertial number for different values of adhesive stiffness ranging from 0 to 0.5 and screw rotational speed of paracetamol-like faceted particles in the screw feeder compared to FT4

The best fitted line on a logarithmic plot obtained for the points in Figure 6 is shown in equation 10.

$$\frac{\tau}{\rho_p d_p^2 \gamma^2} = 3.024 \times I^{-1.80} \quad (10)$$

For values of the Inertial number below 10^{-3} the flow is approximately independent of the shear rate independent, being within the quasi-static regime, while for values of 10^{-3}<I<0.1 the flow falls inside the dense flow regime [9, 10]. It is worth noting that the collapse of the points on to the line is effective not only in the quasi-static regime but also within the intermediate strain rate flow regime, which is defined by the inertial numbers between the two vertical dotted lines in Figure 6, delineating the flow regime boundaries. This trend points towards a possible unified rheology for faceted particles in the screw feeder as is discussed in the following.

4.1.1 Comparison between the screw feeder and the FT4 Rheometer

The Freeman Technology FT4 [21] and Anton Paar [22] powder rheometers are nowadays used increasingly to characterise the bulk powder flow behaviour. A question of great interest is whether the characteristic rheological features of powder flow, as measured by these devices are accountable for bulk powder flow in pieces of process equipment, such as screw feeders. An attempt is therefore made here to analyse the dynamic powder flow in a screw feeder in the same way as it has recently been done for the FT4 instrument by Vivacqua *et al.* [6] for faceted particles.

In FT4 powder rheometer a stainless steel blade moves up and down while rotating inside a powder bed enclosed by a glass tube. A conditioning cycle is run first in order to prepare the bed in a reproducible state. In this first cycle, the blade penetrates the bed while moving clockwise and downwards and then upwards. The shape of the blade induces a gentle slicing and lifting flow pattern which allows a reproducible packing state to be created. In the downward test, the movement induces compression and shearing on the bed as the blade rotates downwards. The measurements in the downward test are obtained by measuring the axial force as well as the torque while the blade rotates anti-clockwise. In this work the small glass cylinder vessel size (25 mm diameter) is simulated, for which the distance between the blade tip and the containing glass wall is 750 μm. The work expended by the blade, termed flow energy, is then calculated and is taken as an indication of the ease with which the bulk powder flows. However, for rheological characterisation it is necessary to calculate the stresses as a function of the strain rate. This has been done by Vivacqua *et al.* [6] using the same non-dimensional stress equation as given by equation 9 as a function of the Inertial number. The results are also shown in Figure 6, where a similar trend prevails, albeit showing different stress levels, illustrating the similarity in the rheological behaviour for the screw feeder and FT4. The slopes of the lines are remarkably similar, whilst the pre-exponential constant differs greatly. The values obtained for

the Inertial number also show the screw feeder to be operating in the quasi-static regime for most of the simulated rotational speeds.

The fluctuations around the regression line in the FT4 are greater than in the screw feeder, where an almost perfect collapse is obtained. This is partly due to the more constant shear rate and stress state of the particles in the screw feeder, while the FT4 is subjected to a higher degree of variations in the values obtained due, in part, to the way the shear rate is obtained as well as to the differential change in depth as the blade moves down. For particle flow in the FT4 (Figure 6), the denominator in the expression for the shear rate was calculated as the maximum translational velocity of the particles, while the average of that velocity was taken instead for the screw feeder. The large fluctuations in maximum velocities if compared to the average are expected to create a higher degree of scattering in the measured values. Averaging the velocity values provides a smoother velocity profile, since it filters spikes in the maximum velocities.

4.2. Analysis of fluctuations in the screw feeder with cohesion and rotational speed

4.2.1. Particle trajectories and velocities

The trajectories of the particles in the screw feeder are shown in Figure 7(a) for spherical shape particles with no adhesion and in Figures 7(b)-(d) for Paracetamol shaped particles with different levels of the adhesive stiffness. Figure 8 illustrates the effect of the rotational speed on the trajectories for $K_{adh} = 0.2$. As evidenced by Figure 7, an increase in the adhesive stiffness results in a higher translational velocity within the screw feeder, presumably as the powder is transported as a packet. In general, the pitches of the screw feeder are filled from the left-hand side of the funnel. As the adhesive stiffness is increased, this trend seems to disappear. This is likely due to the transient arching in the hopper section influencing the way the pitches are filled.

Figure 7: Trajectories of spheres (a) and Paracetamol-shaped particles with different adhesive stiffness values (b)-(f) in the screw feeder at 10 rad/s impeller rotational speed, coloured by translational velocity

Figure 8: Particle trajectories coloured by translational velocity for different rotational speeds with $K_{adh} = 0.2$

Increasing the rotational speed has an effect on the general trend of the velocity magnitudes of the particles without affecting the trajectories so much. As the rotational speed is increased, particles move faster to the left-hand side of the hopper, where the pitches are filled initially, thus creating a slope in the hopper with a rotational speed of 30 rad/s. This effect was investigated previously by Hou *et al.* [1], where four different simulations of the same bin with different lengths of the screw feeder were analysed. Depending on the length of the screw inside the container a different drawdown pattern was encountered. However, in the present work, no recirculation of particles was found in the simulations independent of the velocity of the screw. This might be related to both the faceted shapes of the particles being simulated in this work as well as the adhesion introduced in the system. Additionally, a longer length of the screw underneath the hopper would result in a higher slope of the drawdown pattern [1]. If the length was short, the sign of the slope would be inverted, as the particles would be drawn towards the outlet of the funnel (or the inlet of the tube where screw feeder is placed). These can be considered a consequence of how the pitches of the screw are filled. In the cases analysed here the pitches are filled first on the left-hand side so that, when the material in the

pitch is pushed forward, the pitch on the right-hand side is already full, thus having no more room for further drawdown.

4.2.2 Mass flow rate

In the simulations, the hopper is first filled with particles and then the rotation of the screw is started. A certain amount of time after that, which varies for each K_{adh} and rotational speed, particles start to come out of the screw feeder. The flow was allowed to stabilise before measurements were taken. The first step in the simulation was the filling of the hopper, after which the screw was set to start rotating. This causes an initial transient state until the particles settle and the stresses stabilise. After around 2 s of simulation the levels of the stresses in the particles started to oscillate around a mean value, following which the measurements were taken.

For screw feeders with pitches of equal length the quantity discharged by a single pitch can be defined by the mass that leaves the screw feeder in one rotation of the screw. Once the particles start to exit the screw feeder, the simulation time is expressed in terms of the number of pitch discharged. This method allows monitoring how much material is coming out of the screw feeder and how stable the flow rate is, as well as its dependency on surface energy and rotational speed. This operation was carried out for the performed simulations and the results are shown in Figure 9. At a glance, the simulation with the highest surface energy for Paracetamol can be easily identified. At an adhesive stiffness of 0.5, the mass discharged is notably lower if compared to the rest of the cases. This may be seen initially to be at odds with trends shown in Figure 8, where an increase in the adhesive stiffness results in a higher translation velocity within the screw feeder. However, as the results shown in Figure 9 are on the mass basis, the trend implies incomplete filling of the pitches. In all cases, the mass

discharged per screw feeder pitch exhibits a similar degree of variability with a lowering average of discharged mass as the adhesive stiffness is increased.

Figure 9: Discharged mass for each individual pitch of the screw feeder for different surface energies and rotational speeds. (a): spheres; (b)-(h): Paracetamol shaped particles with different adhesive stiffness values

The average mass discharged per pitch, obtained for each of the sequences in Figure 9 at 10 $\frac{rad}{s}$ is shown in Figure 10. Despite the mentioned variability within the same simulation in terms of the individual mass discharged per pitch, when looking at the averages for each value of the adhesive stiffness, a general trend can be identified. The calculated averages decrease almost linearly as the adhesive stiffness is increased. There is, however, a value of the adhesion for which the mass discharged becomes null (not shown here). For the Luding contact model used in this work [32, 33], at a value of the adhesive stiffness of 0.7, no mass flow rate is detected at the outlet. This is due to most of the particles being expelled out of the domain due to the high cohesive forces and interactions with the walls. The few particles that entered the screw feeder remain attached to the walls of the domain, hence no mass exiting it. This decrease in the average mass discharged is influenced, in part, by a higher void fraction as the adhesion forces become higher. The effect of the adhesion forces on the bed void fraction is highlighted in Figure 11. The void fraction is monitored in two cuboid volumes (c.f. Figure 5). The increase in the void fraction for cuboid 1, which is placed directly below the hopper, is notably smaller than for cuboid 2. This difference is due to the weight of particles inside the hopper, resulting in an increase of the packing fraction in cuboid 1. Cuboid 2 instead is observed to have a steeper

increase in the void fraction as the adhesive stiffness increases, as in this case there is no surcharge.

Figure 10: Average discharged mass for each individual pitch of the screw feeder for different surface energies and rotational speeds. Standard deviation for each of the series with increasing adhesion level is 5.55%, 5.60%, 6.50%, 10.45%, 13.83% and 7.21%

Figure 11: Average void fraction as a function of the adhesive stiffness for a rotational speed of 10 rad/s

In another analysis, the variation of the average void fraction is analysed as a function of the rotational speed and the results are shown in Figure 12. The higher rotational speed of the screw allows for less time of the individual pitches to be filled with particles, which results in a higher void fraction as the speed is increased. The particle weight in the hopper appears to have a clear effect on the trend of the voidage. As suggested previously [1], the rotational motion of the screw tends to generate larger voids between particles. These voids are not successfully filled as a result of the cohesive forces in a confined environment, especially inside Cuboid 2 in the screw feeder, where there are no additional compressive forces (such as the hydrostatic pressure induced by the particles inside the hopper for Cuboid 1) producing an increase in the packing fraction. A more detailed analysis of contact force relaxation as influenced by adhesion is needed to develop a deeper understanding.

Figure 12: Average void fraction as a function of rotational speed for K_{adh}=0.2 for inspection cuboids

4.2.3. Power consumption

Energy consumption is calculated here to explore its link with adhesion. By dividing the mass discharged in one screw revolution by the energy used, the energy utilisation in the screw feeder as a function of the adhesive stiffness is obtained and is shown in Figure 13. A steep reduction in the mass discharged per unit power input is observed as the adhesive stiffness is increased. The trend can be approximated accurately by an exponential function, as shown by equation 13 in terms of the adhesive stiffness.

$$Average\ mass\ discharged\ per\ Watt = 330.2\ e^{-10.82K_{adh}} \quad (13)$$

Figure 13: Average mass discharged (mg) per Watt consumed as a function of the adhesive stiffness

The average mass discharged per unit power (i.e. the energy utilisation) as a function of the rotational speed of the screw for an adhesive stiffness of 0.2 is shown in Figure 14. The limited data points suggest that beyond a certain speed the energy utilisation remains constant.

Figure 14: Average mass discharged (mg) per Watt consumed as a function of the rotational speed for K_{adh} = 0.2

4.3. Analysis of the instabilities in the screw feeder

Arching

Two simulations with adhesive stiffness 0.5 were run for Paracetamol-shaped particles with the cumulative particle size distribution shown in Table 4. In both cases, the hopper was initially filled for 2 s after which the rotation of the screw feeder (10 rad/s) was initiated. In order to be able to look at the arch formation and development, a parallelepiped was constructed excluding the particle layers closest to the walls, showing only a width of around 7 particle diameters inside the hopper.

The first simulation was run for 10 s and the particle inlet was stopped after 2 s while the second simulation included a second inlet with a continuous inlet mass flow rate equal to the average discharged. In order to calculate the average mass, the total mass discharged was divided by the time during which particles were continuously reaching the outlet. Transient arching was detected in both simulations taking place, however at different heights inside the hopper. Figure 15(a) shows the arch detected for the first case while Figures 15(b) and 15(c) show the arches occurring in the second simulation. The arch in Figure 15(a) started to form around 4.5 s into the simulation and grew to its maximum size at around 9 s of simulation. It stayed stable for 0.8 s after which it partially collapsed. This unstable arch finally failed at 10.07 s of simulation. The arch shown in Figure 15(b) started its formation after 4.85 s, increasing progressively in size until it partially failed. However, instead of collapsing

completely as in the previous case, the arch moved upwards inside the hopper until the force chains became stable again and it started growing again to approximately twice its initial size. Three snapshots of this sequence are shown in Figures 15(b), (c) and (d).

Figure 15: Arching of paracetamol-shaped particles for an adhesive stiffness of 0.5 in two different simulations

Flow irregularities

Stable arching is obviously catastrophic for screw feeders. However, in handling cohesive powders transient arching can occur and has deleterious effect on smooth flow. It prevents complete filling of the screw feeder pitches, giving rise to irregularities in the flow. This is predictable as shown in Figure 16. The increase in the void fraction shown in Figure 11 as the adhesive stiffness is increased is not only due to uniform increase in the interstitial voidage, but also due to cavities formed by transient arching, as visualised in Figure 16.

Figure 16: Irregular filling of the screw feeder pitches giving rise to unstable mass flow rate at the outlet. Left: K_{adh}=0.3 and Right: K_{adh}=0.5

5. Conclusions

Powder flow of faceted particles in a screw feeder has been analysed and a rheological model for the flow of cohesive faceted particles in screw feeders has been developed relating the prevailing shear stress to the strain rate.

The mass flow rate through the screw feeder has been calculated and expressed as a function of the adhesive stiffness and screw rotational speed. The flow becomes increasingly irregular while the average mass carried per pitch decreases almost linearly with increasing adhesive stiffness. Void fraction in the screw feeder increases with both speed of the screw and adhesive stiffness.

The required power for pushing a certain mass through the feeder has been calculated as influenced by adhesion and screw rotational speed. The results are presented in terms of the average mass discharged per unit power input (energy utilisation). They show an exponential decrease as the adhesive stiffness is increased. When the effect of rotational speed is considered, the energy utilisation decreases first as the speed is increased, but at high speeds it does not change any further.

Transient arching is detected for two different cases with and without continuous feeding in the hopper. The adhesive stiffness for which arching is detected is 0.5 and it is noted that the unstable arch moves within the hopper when continuous feeding is applied. This movement is produced by successive collapses and rebuilds of the arch. Intermittencies in the flow are greatly influenced by the cohesive forces, which prevent the complete filling of the pitches, thus giving rise to both irregular flow as well as a reduced output. Transient cohesive arching merits further study to draw a regime map based on particle properties, screw feeder geometry and rotational speed.

6. Acknowledgements

The authors gratefully acknowledge the funding provided by the Advanced Manufacturing Supply Chains Initiative (AMSCI) and the Medicines Manufacturing Industry Partnership (MMIP) as well as the industrial collaborators in the Advance Digital Design of Pharmaceutical Products (ADDoPT) project. The numerical simulations were carried out using Rocky DEM software package provided by ESSS under an academic license.

7. References

[1] Hou, Q.F., Dong, K.J. and Yu, A.B., DEM study of the flow of cohesive particles in a screw feeder, Powder Technology 256 (2014), pp. 529-539.

[2] Jenike, A. W., Gravity flow of bulk solids, Bulletin 108, Utah University (1961)

[3] Jenike, A. W., Storage and flow of solids, Bulletin 123, Utah University (1964)

[4] Walker, D. M., An approximate theory for pressures and arching in hoppers, Chemical Engineering Science 21 (1966), pp. 975-997

[5] Enstad, G., On the theory of arching in mass flow hoppers, Chemical Engineering Science 30 (1975), pp. 1273-1283

[6] Vivacqua., V., López, A., Hammond, R., Ghadiri, M., DEM analysis of the effect of particle shape, cohesion and strain rate on powder rheometry, Powder Technology 342 (2019) pp. 653-663.

[7] Campbell, C. S., Granular shear flows at the elastic limit, Journal of Fluid Mechanics, 465 (2002), pp. 261-291

[8] Jop, P., Forterre, Y, Pouliquen, O., A constitutive law for dense granular flows. Nature 441 (2006), pp.727-730

[9] Tardos, G.I., McNamara S., Talu I., Slow and intermediate flow of a frictional bulk powder in the Couette geometry, Powder Technol. 131 (2003) pp. 23–39.

[10] Berger, N., Azéma, E., Douce, J. F., Radjai, F., Scaling behaviour of cohesive granular flows, EPL 112 64004 (2015), pp. 1-6

[11] Parrella, L., Barletta, D., Boerefijin, R., and Poletto, M., KONA 26 (2008), pp. 178-189.

[12] Bell, A.T., Evaluation of Edinburgh Powder Tester, PARTEC, Nuremburg, Germany, 2007.

[13] Hassanpour, A. and. Ghadiri, M., Particle & Particle Systems Characterization 24 (2007), pp. 117-123

[14]Schulze, D., "A new ring shear tester for flowability and time consolidation measurements" in International Particle Technology Forum, 1st International Particle Technology Forum, USA, 1994, pp. 11-16

[15] Calvert, G., Curcic, N., Redhead, C., Ahmadian, H., Owen, C., Beckett, D., & Ghadiri, M., A new environmental bulk powder caking tester. Powder Technology, 249 (2013), pp. 323-329.

[16] Girimonte, R., Bernardo, P., Minnicelli, A., Formisani, B., Experimental characterization of the cohesive behaviour of fine powders by the raining bed test, Powder Technology, 325 (2018), pp. 373-380.

[17] Castellanos, A., Valverde, J.M., Quintanilla, M.A.S., The Sevilla Powder Tester: A tool for characterizing the physical properties of fine cohesive powders at very small consolidations, KONA Powder and Particle Journal, 22 (2004), pp. 66-81.

[18] Berry, R.J., Bradley, M.S.A., McGregor, R.G., Brookfield powder flow tester – Results of round robin tests with CRM-116 limestone powder, Proceedings of the Institution of Mechanical Engineers, Part E: Journal of Process Mechanical Engineering, 229 (2014), 215-230.

[19] Hosokawa Micron Powder Tester PT-X, Standard Test Method for Bulk Solids Characterization by Carr Indices, ASTM International Designation: D 6393 – 08.

[20] Johanson, K., SSSpinTester-X Powder Strength Tester, Material Flow Solutions, Inc., https://www.matflowsol.com/images/PDF/products/SSSpinTester/Full%20Brochure.pdf, (2019).

[21] Freeman, R., Measuring the flow properties of consolidated, conditioned and aerated powders – a comparative study using a powder rheometer and a rotational shear cell. Powder Technology 174 (2007), pp. 25–33.

[22] Salehi, H., Sofia, D., Schütz, D., Barletta, D., Poletto, M., Experiments and simulation of torque in Anton Paar powder cell, Particulate Science and Technology 36:4 (2018), pp. 501-512

[23] Hare, C., Zafar, U., Ghadiri, M., Freeman, T., Clayton, J., Murtagh, M.J., Analysis of the dynamics of the FT4 powder rheometer. Powder Technology, 285 (2015), pp.123–127.

[24] Nan, W., Ghadiri, M., Wang, Y., Analysis of powder rheometry of FT4: Effect of air flow, Chemical Engineering Science, 162 (2017), pp. 141-151

[25] Polizzi, M.A., Franchville, J., Hilden, J. L., Assessment and predictive modelling of pharmaceutical powder flow behaviour in small scale hoppers, Powder Technology 294 (2016), pp. 30-42

[26] Karde, V., Ghoroi, C., Fine powder flow under humid environmental conditions from the perspective of surface energy, International Journal of Pharmaceutics, 485 (2015), pp. 192-201.

[27] Li, M., Leturia, M., Saleh, K., Analysis of the periodic motion in a powder rheometer and development of a new Flowability testing method, Kona Powder and Particle Journal 34 (2017), pp. 1-11

[28] Siliveru, K., Jange, C. G., Kwek, J. W., Ambrose, R. P. K., Granular bond number model to predict the flow of fine flour powders using particle properties, Journal of Food Engineering 208 (2017), pp. 11-18

[29] Pantaleev, S., Yordanova, S., Janda, A., Marigo, M., Ooi, J. Y., An experimentally validated DEM study of powder mixing in a paddle blade mixer, Powder Technology 311 (2017), pp. 287-302

[30] Nan, W, Ghadiri, M, Wang, Y, Analysis of powder rheometry of FT4: Effect of particle shape, Chemical Engineering Science, 173 (2017), pp. 374-383

[31] Cundall, P.A., Strack, O. D. L., A discrete numerical model for granular assemblies, Géotechnique 29 (1979), pp. 47-65.

[32] Rocky 3, Technical Manual, Rocky DEM, ESSS, Florianopolis, Brazil (2017).

[33] Lommen, S., Schott, D., Lodewijks, G., DEM speedup: Stiffness effects on behaviour of bulk material, Particuology 12 (2014), pp. 107-112.

[34] Luding, S., Cohesive, frictional powders: contact models for tension, Granular Matter (2008) 10:235–246.

[35] Abeyaratne, R. Continuum Mechanics: Volume II of Lecture notes on the mechanics of elastic solids, Electronic publication (2012), MIT Department of Mechanical Engineering, http://web.mit.edu/abeyaratne/lecture notes.html

[36] Hare, C., Zafar, U., Ghadiri, M., Freeman, T., Clayton, J., Murtagh, M.J., Analysis of the dynamics of the FT4 powder rheometer. Powder Technology 285 (2015), pp. 123-127.

[37] Remy, B., Khinast, J.G., Glasser, B.J., Discrete Element Simulation of Free Flowing Grains in a Four-Bladed Mixer. AICHE Journal, 55 (2009), pp. 2035-2048.

[38] Remy, B., Khinast, J.G., Glasser, B.J., Polydisperse granular flows in a bladed mixer: Experiments and simulations of cohesionless spheres. Chemical Engineering Science 66 (2011), pp. 1811-1824.

Table 1: Parameters used for construction of the faceted particles

Parameter	Value
Shape type	Faceted
Vertical aspect ratio	1
Horizontal aspect ratio	1.25
Number of corners	15
Superquadratic degree	5

1

Table 2: Material properties for paracetamol and stainless steel

Material property	Particles	Geometry
Density (kg/m^3)	800	2500
Young's modulus (GPa)	0.1	0.1

2

Table 3: Interaction coefficients for particles and boundaries

Interaction property	Particle-particle	Particle-Geometry
Restitution coefficient	0.8	0.8
Static friction coefficient	0.4	0.5
Dynamic friction coefficient	0.4	0.5

3

4

Table 4: Cumulative particle size distribution

Size (Equivalent volume diameter [µm])	Cumulative % Undersize
625	100
600	75
550	50
500	30
450	10
400	1

5

6

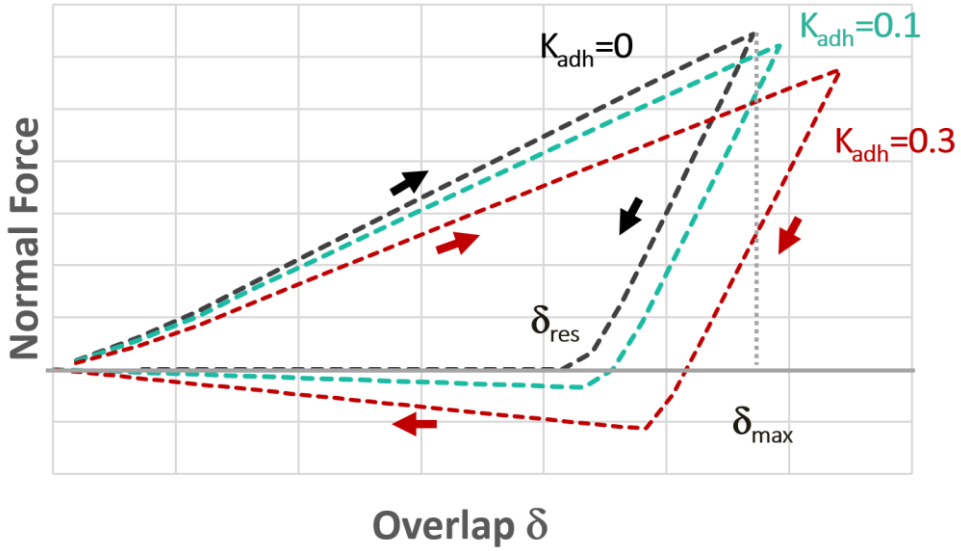

Figure 1: Force-Overlap graph for different values of the adhesive stiffness obtained in Rocky DEM for a spherical particle against a wall

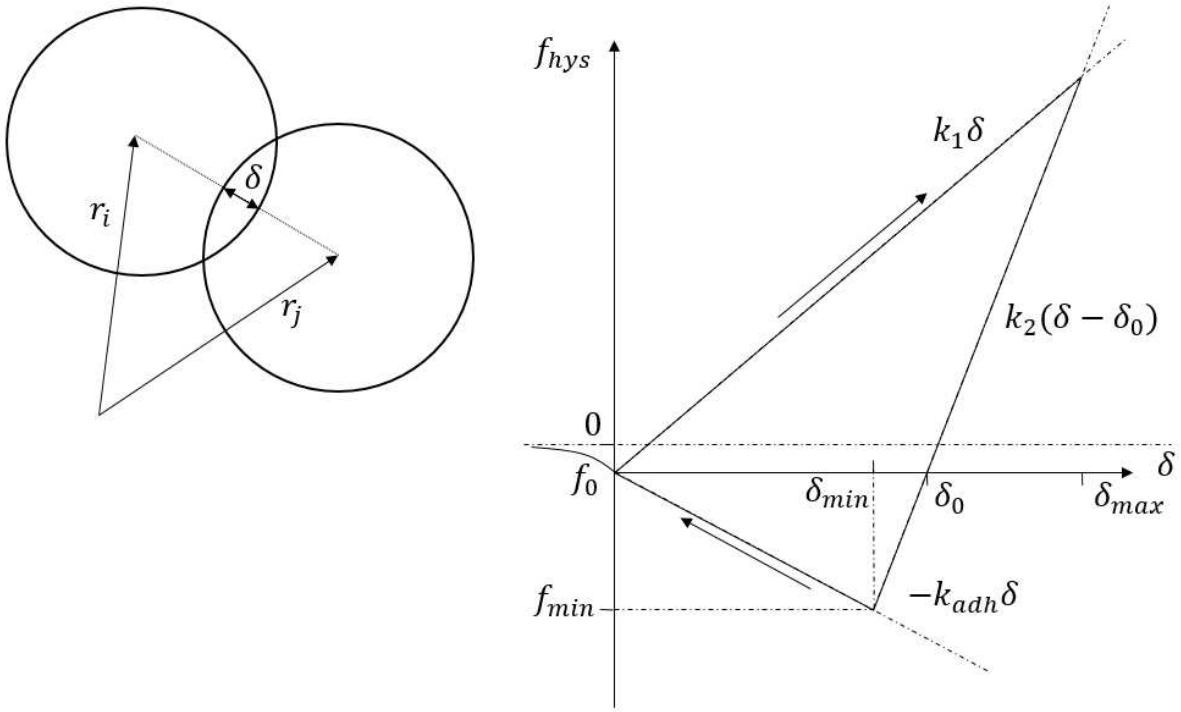

Figure 2: Luding's elasto-plastic adhesive contact model redrawn from [29]

1
2

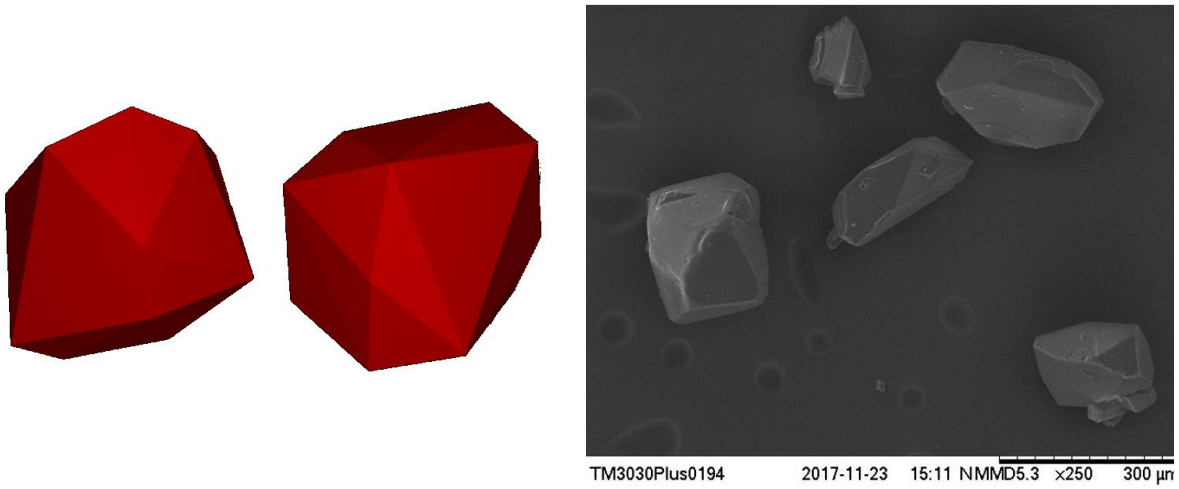

(a) **(b)**

Figure 3: (a) Shape of the faceted particles selected for the simulations in Rocky DEM and (b) SEM image of paracetamol crystals

1

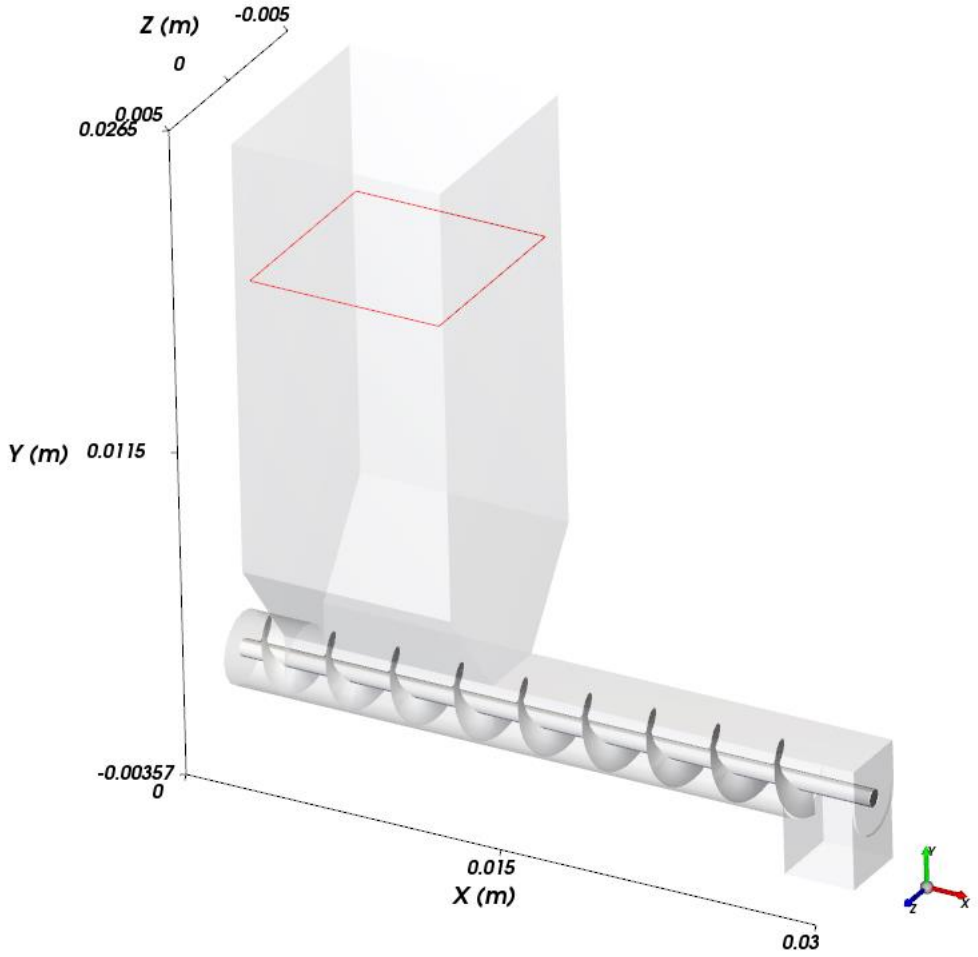

Figure 4: Geometry of the screw feeder used in the simulations

2

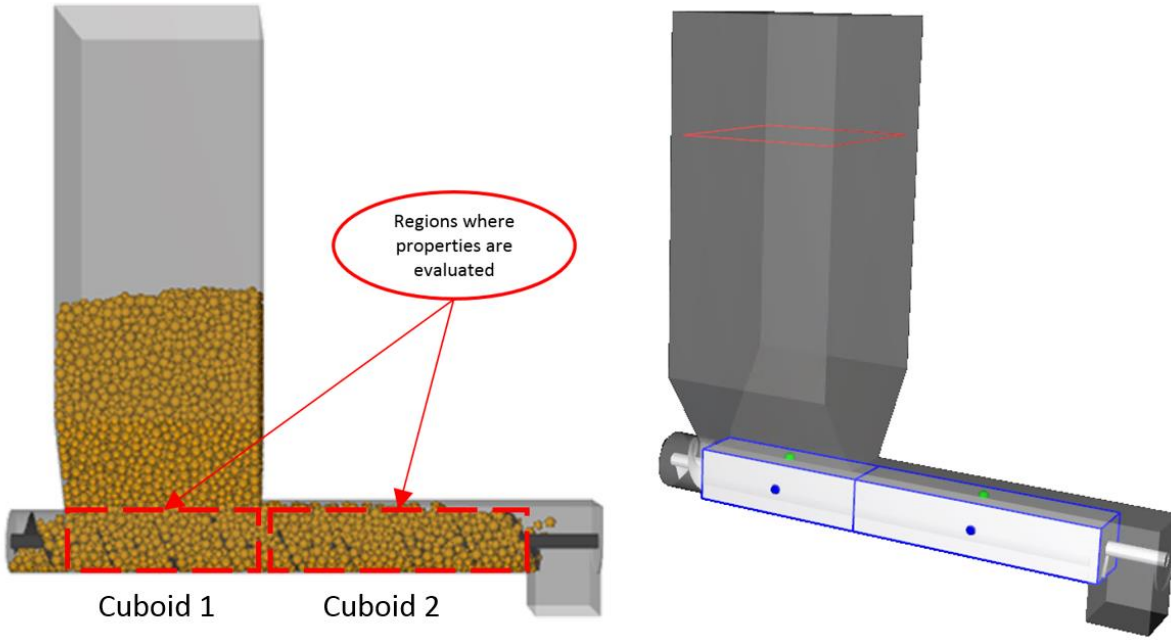

Figure 5: Representation of the measurement volumes in the screw feeder

1

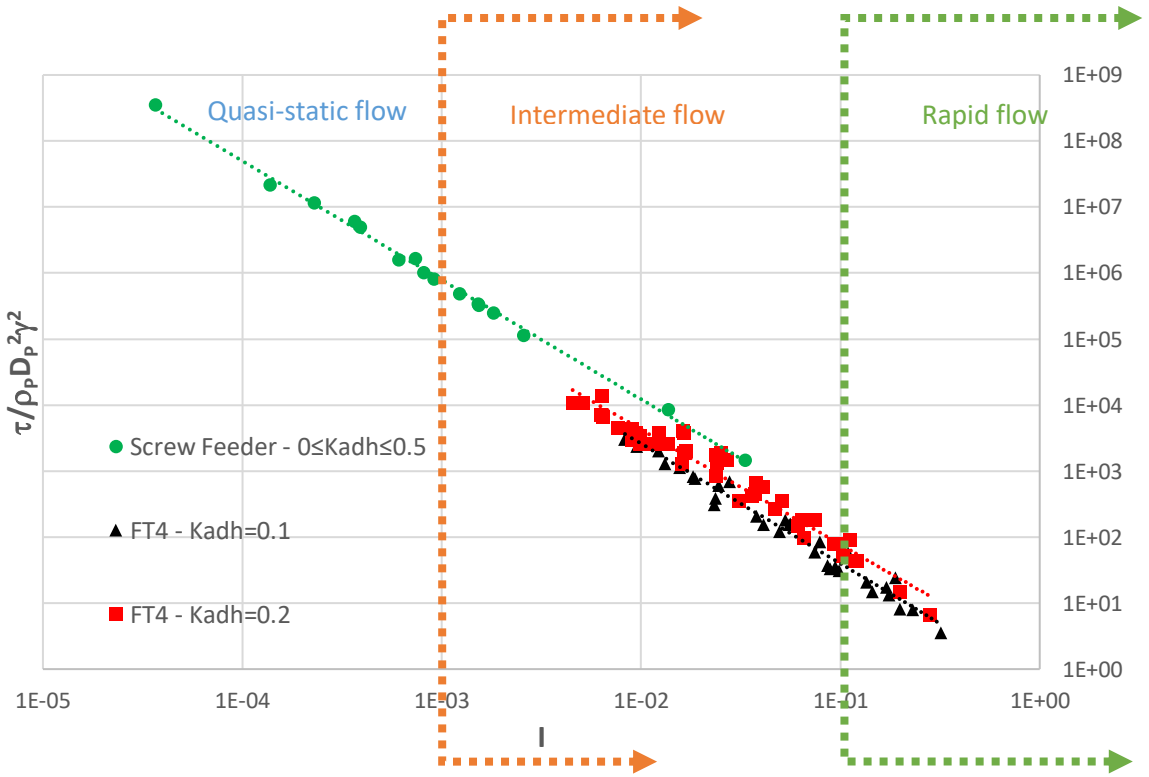

Figure 6: Non-dimensional stress as a function of the Inertial number for different values of adhesive stiffness ranging from 0 to 0.5 and screw rotational speed of paracetamol-like faceted particles in the screw feeder compared to FT4

2

1

2

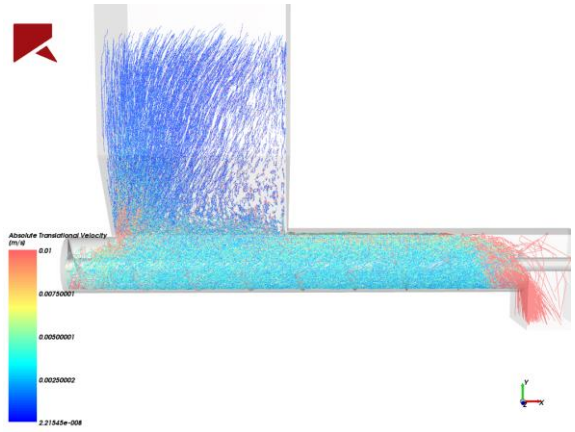

(a) Kadh = 0

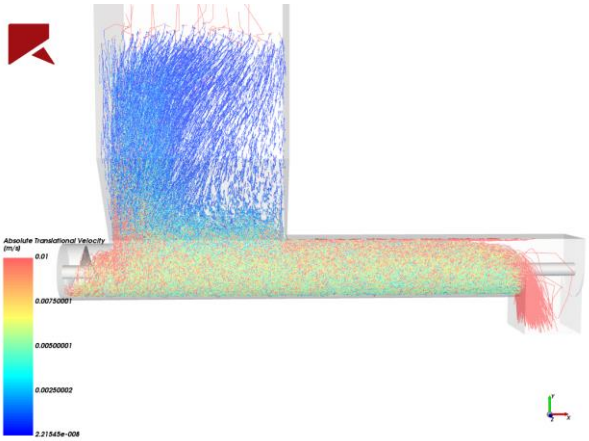

(b) Kadh = 0.1

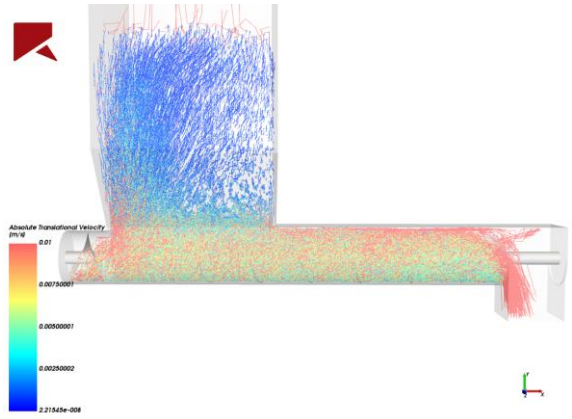

(c) K_{adh} = 0.15

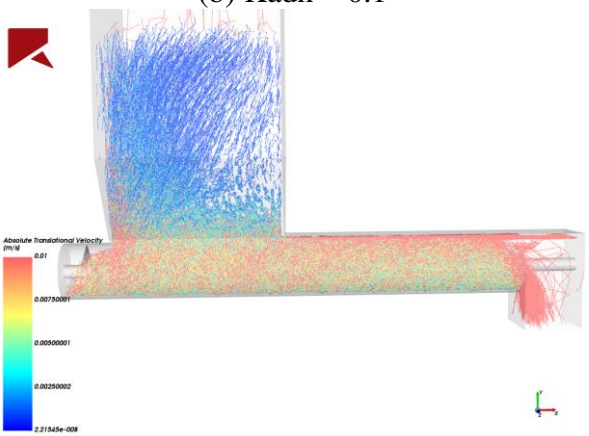

(d) K_{adh} = 0.2

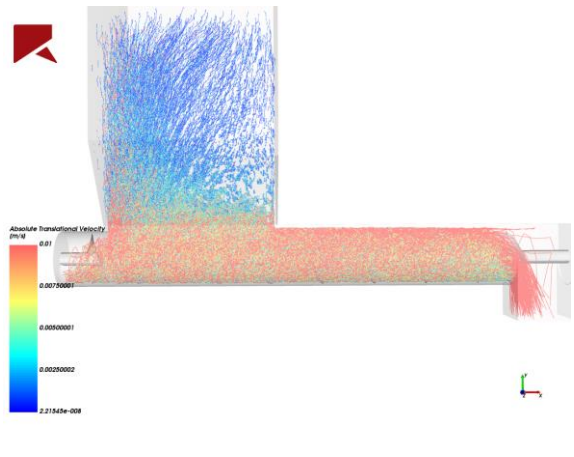

(e) K_{adh} = 0.3

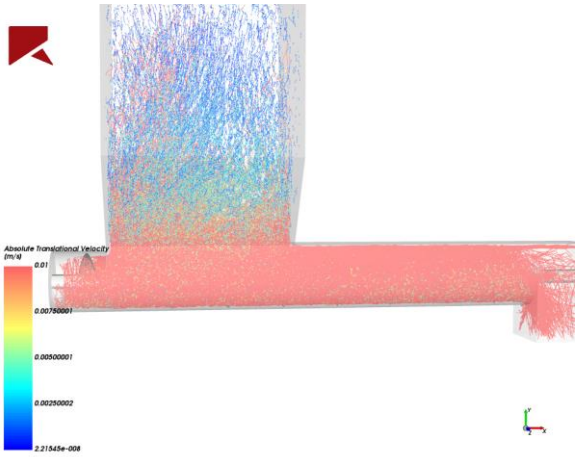

(f) K_{adh} = 0.5

Figure 7: Trajectories of spheres (a) and paracetamol-shaped particles with different adhesive stiffness values (b)-(f) in the screw feeder at 10 rad/s impeller rotational speed, coloured by translational velocity.

1

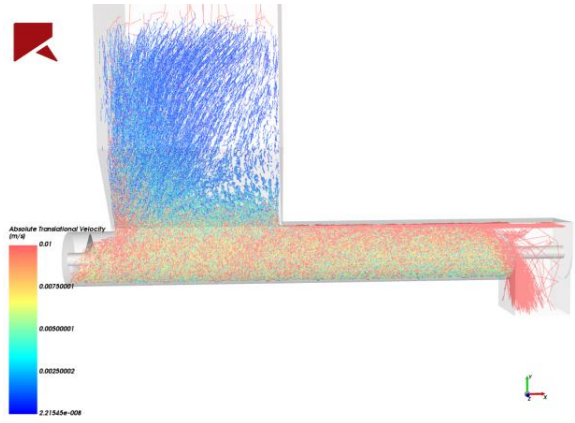

Paracetamol ω = 10 rad/s

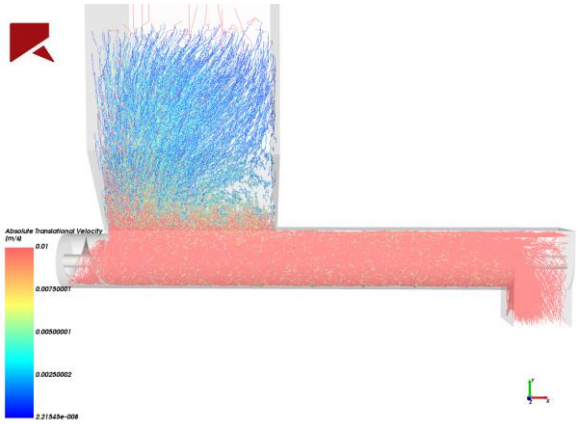

Paracetamol ω = 20 rad/s

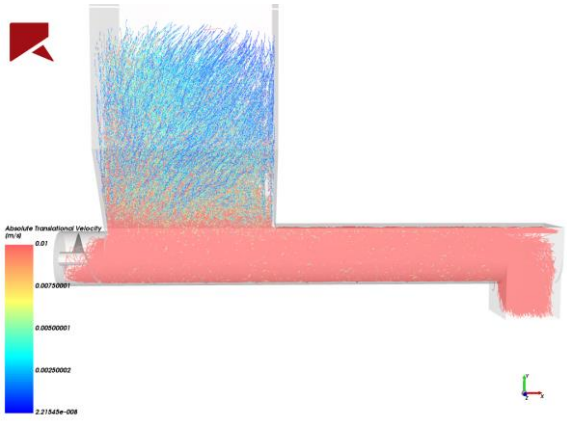

Paracetamol ω = 50 rad/s

Figure 8: Particle trajectories coloured by translational velocity for different rotational speeds with K_{adh} = 0.2

2

3

4

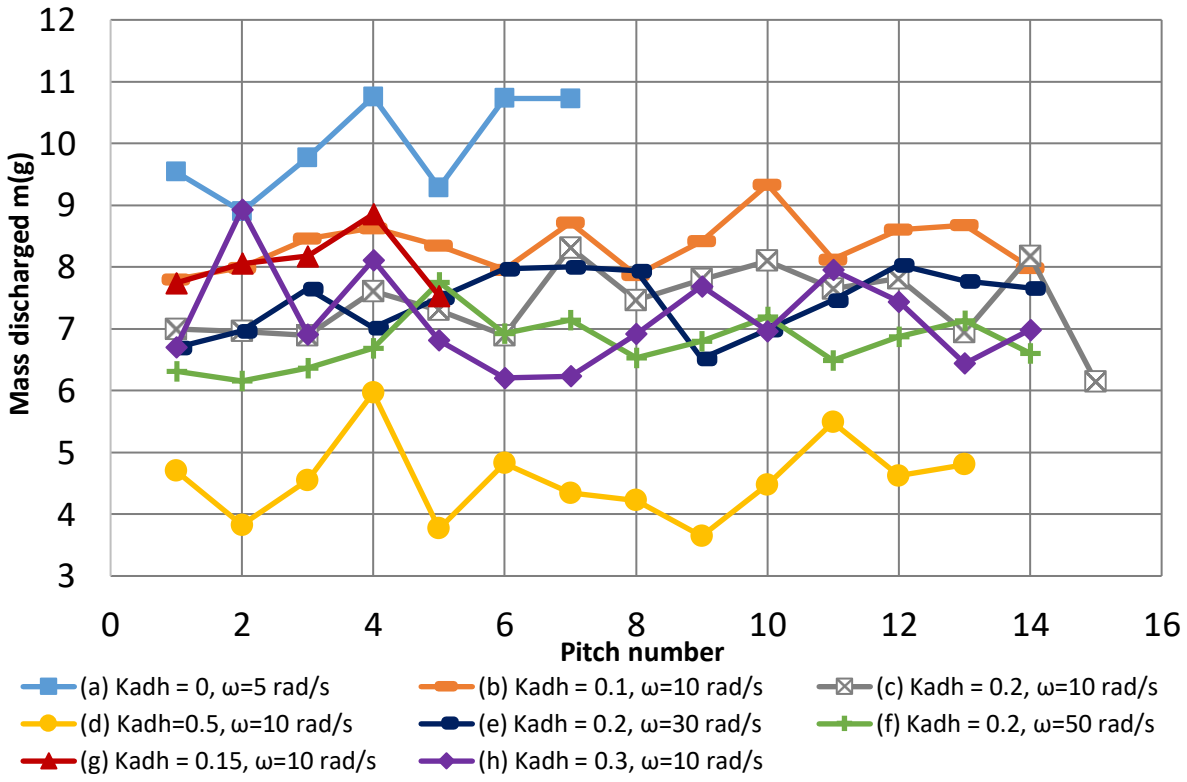

Figure 9: Discharged mass for each individual pitch of the screw feeder for different surface energies and rotational speeds. (a): spheres; (b)-(h): Paracetamol shaped particles with different adhesive stiffness values

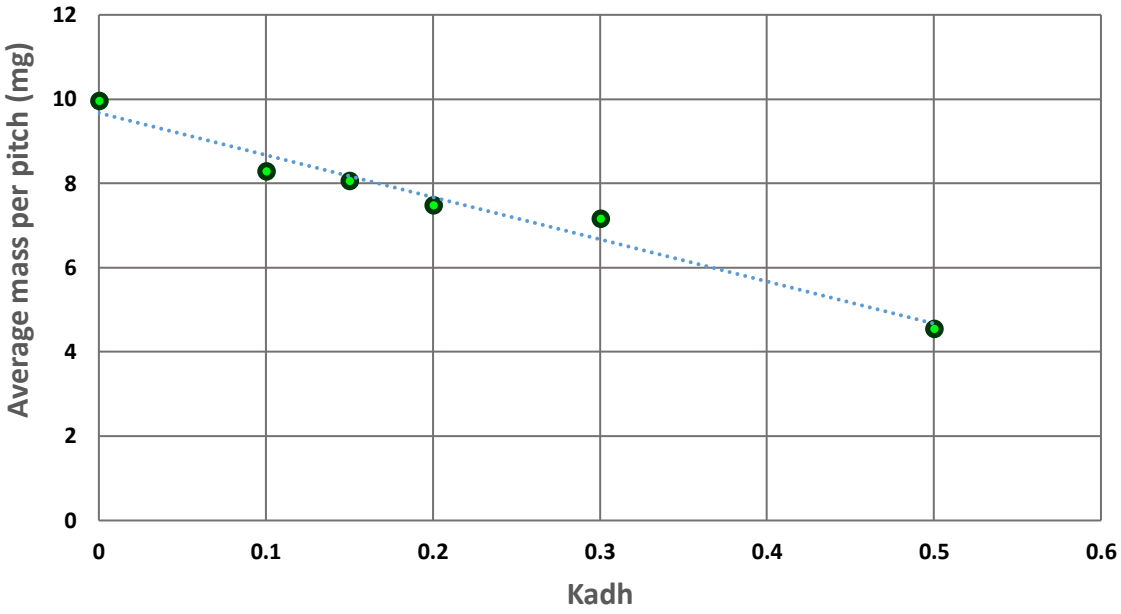

Figure 10: Average discharged mass for each individual pitch of the screw feeder for different surface energies and rotational speeds. Standard deviation for each of the series with increasing adhesion level is 5.55%, 5.60%, 6.50%, 10.45%, 13.83% and 7.21%

1

2

3

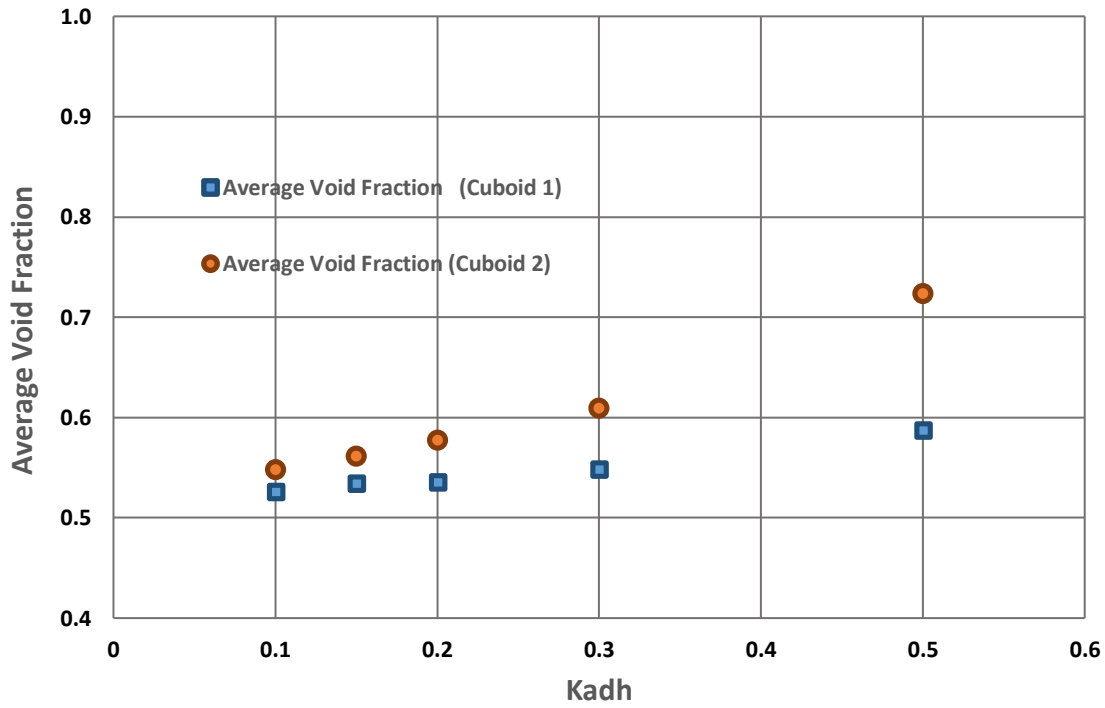

Figure 11: Average void fraction as a function of the adhesive stiffness for a rotational speed of 10 rad/s

4

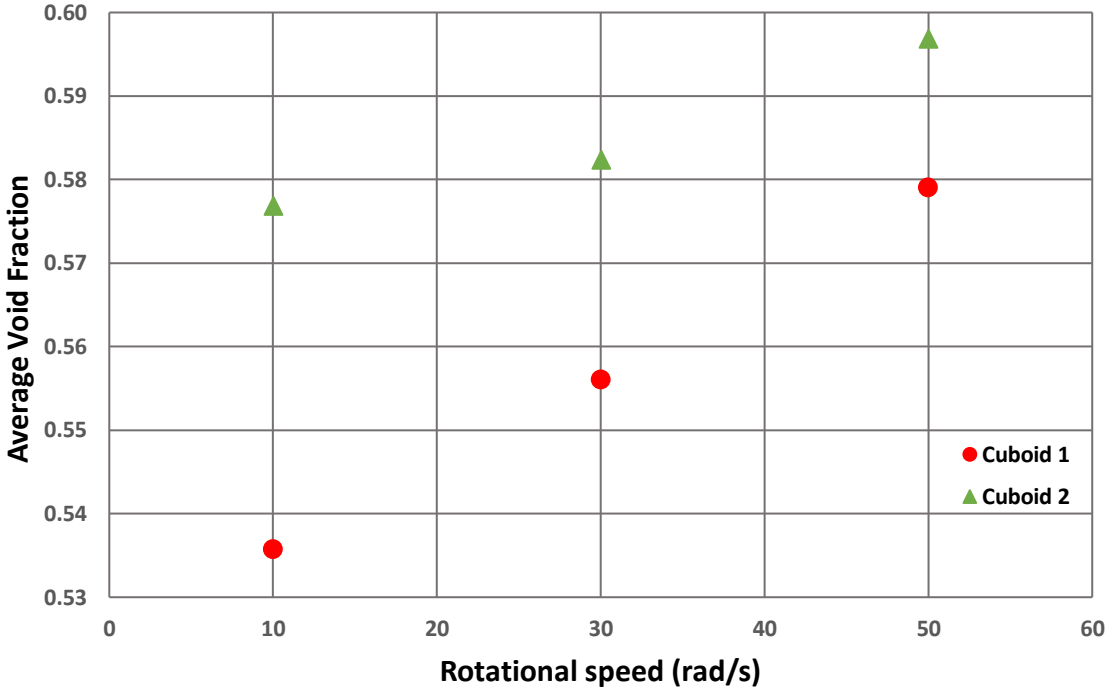

Figure 12: Average void fraction as a function of rotational speed for K_{adh}=0.2 for inspection cuboids

1

2

3

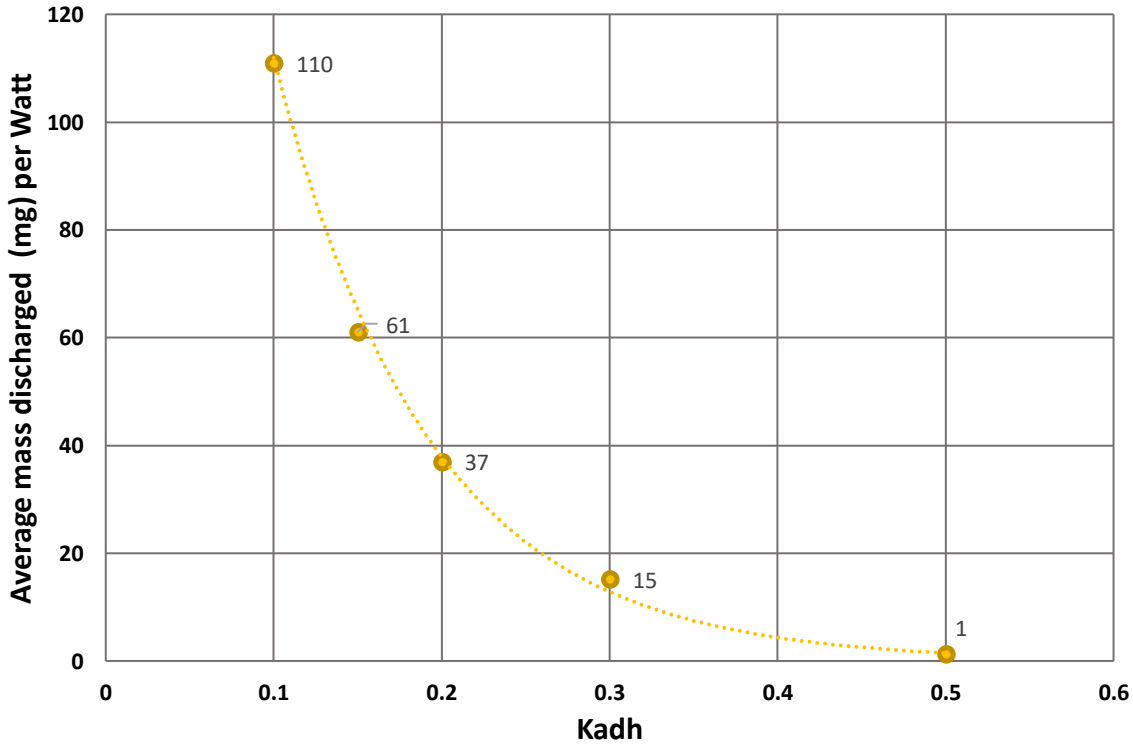

Figure 13: Average mass discharged (mg) per Watt consumed as a function of the adhesive stiffness

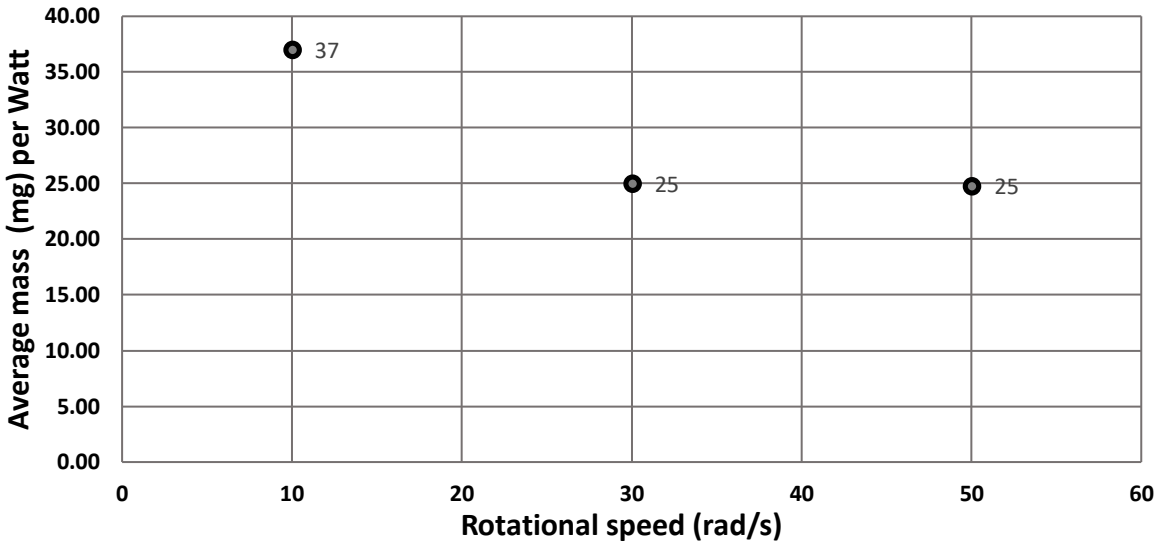

Figure 14: Average mass discharged (mg) per Watt consumed as a function of the rotational speed for K_{adh} = 0.2

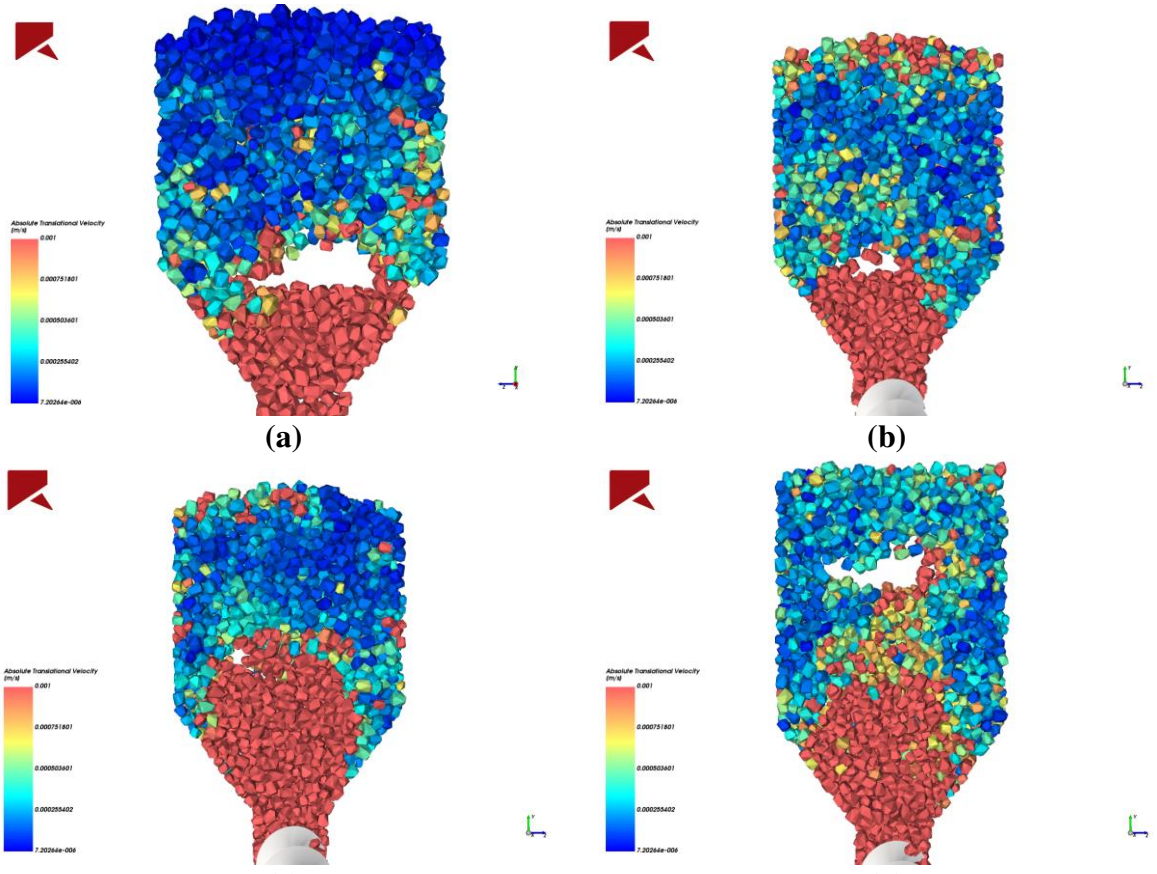

Figure 15: Arching of Paracetamol-shaped particles for an adhesive stiffness of 0.5 in two different simulations

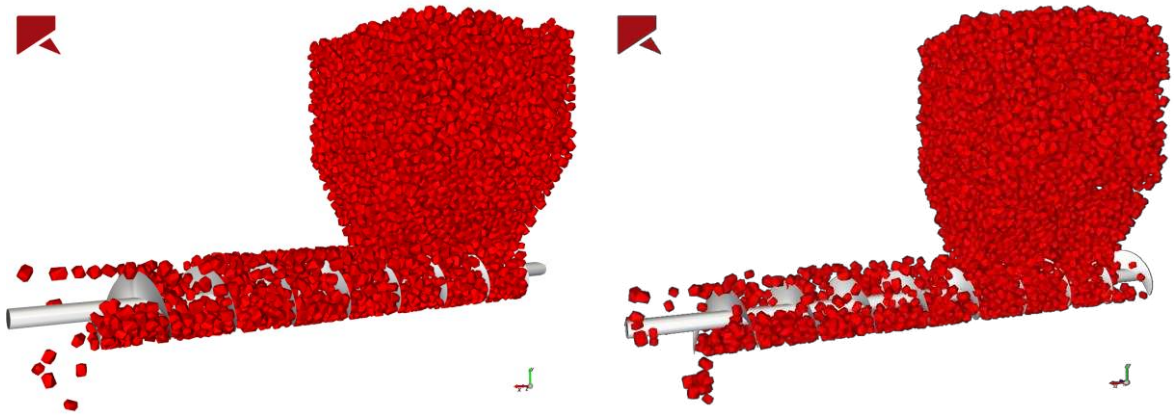

Figure 16: Irregular filling of the screw feeder pitches giving rise to unstable mass flow rate at the outlet. Left: K_{adh}=0.3 and Right: K_{adh}=0.5

1

2